Universal diagram for the kinetics of particle deposition in microchannels

Cesare M. Cejas,[1,*] Fabrice Monti,[1] Marine Truchet,[1] Jean-Pierre Burnouf,[2] and Patrick Tabeling[1]

[1]*Microfluidics, MEMS, Nanostructures Laboratory, CNRS Gulliver UMR7083, Institut Pierre Gilles de Gennes (IPGG), ESPCI Paris, PSL Research University, 6 rue Jean Calvin, Paris 75005, France*

[2]*PDP-Predevelopment Sciences Early Development, Sanofi Recherche, 13 quai Jules Guesdes, BP 14, Vitry-sur-Seine 94403, France*

(Received 25 April 2018; revised manuscript received 8 September 2018; published 10 December 2018)

Why do particles, suspended in a fluid and traveling in a channel, deposit onto walls? The question has far-reaching implications in different domains (filtering, syringeability, fouling, etc.). Close to a channel wall, particles are subject to a variety of effects, which control their trajectories: hydrodynamic forces, diffusion, van der Waals adhesion forces, and electrostatic forces. The existing theories and phenomenologies, due to their inherent limitations, and the numerical and experimental studies, due to their scarcity, did not allow thus far to establish a general description of the deposition process. By coupling microfluidic experiments, theory, and numerics, we succeed in establishing a general description of the phenomenon. We discover that the problem is particularly rich. We show the existence of three regimes: van der Waals, Debye, and diffusive, each including various subregimes. Within each main regime, particle deposition is dominated respectively by (attractive) van der Waals forces, (repulsive) electrostatic forces, or diffusion. We establish the scaling laws governing the collector efficiency, S, in each regime. The ensemble of the regimes and their transitions can be displayed in diagrams. We focus on the case $\frac{A}{kT} \sim 1$ (the case of most practical interest), in which the diagram involves two dimensionless numbers, P (incorporating the Debye layer characteristics) and ξ_L (a function of the flow speed, diffusion constant, and the geometry). In this case, the three main regimes organize around a cantilever beam, in which the vertical support is defined by the condition $P = 4e^{-2}$, and the horizontal beam is located at $\xi_L = \frac{A}{kT}$, where A, k, and T are the Hamaker constant, the Boltzmann constant, and the absolute temperature, respectively. The present work allows understanding of empirical observations thus far left unexplained and provides a paradigm enabling engineering of devices in a way that reduces or enhances particle deposition.

DOI: 10.1103/PhysRevE.98.062606

I. INTRODUCTION

Particle deposition on solid walls represents one of the few phenomena, in physics, where kinetics is controlled by a large range of scales, extending from the intermolecular scale to the size of the system in which the suspension is driven, thus spanning several decades. Particle deposition is involved in many applications, in a favorable, unfavorable, and sometimes catastrophic manner. To mention a few examples, in membrane filtration, particle deposition is exploited to retain solid matter [1]; in the pharmaceutical industry, it is minimized for efficient medical administration in syringe needles [2]. In the oil industry, asphaltene deposition in reservoirs reduces or even blocks the production [3]. In most situations, the prolonged deposition of individual colloidal particles on naked surfaces leads to the eventual accumulation of multiple layers that often cause clogging [1,4–7], which results in loss of permeability [8] in confined geometries (microchannels and pores) [9] or complete obstruction of suspension flow [3,6,7]. Clogging leads to particulate fouling, which evidently reduces efficiency [10] and even loss of the device [2].

Over the last three decades, a number of theoretical, numerical, and experimental investigations have been undertaken [5,11–13]. However, for a long time, theoretical studies addressed situations difficult to substantiate experimentally, modeling was heavily phenomenological, and the numerical and experimental work provided descriptive studies from which it was challenging to extract information of broad interest. Recently, with the development of microfluidics, a new generation of experimental studies has been conducted, providing well-documented analyses of deposition kinetics of colloidal polystyrene (PS) spheres on surface walls of microchannels with flows driven by pressure gradients or electrokinetic forces [6,7,11,12,14,15]. In addition, studies on particle deposition as a precursor to clogging phenomena [1,4,5,14–16] have been undertaken. These studies have generated substantial amounts of well-controlled data; as a whole, they reported interesting information in specific cases and, in the meantime, underlined the complexity of the phenomenon. Still, they were essentially descriptive or phenomenological and, with them, it is difficult to establish a general picture of the phenomenon.

Deposition involves diffusion, advection, adhesion, electrostatics, geometry, and confinement; it is therefore a complicated phenomenon, somehow reflected by the descriptive level of the literature. As previously mentioned, the phenomenon involves a range of scales spanning several decades, from the size of the channels through which the suspension is driven to the nanometric scales of the intermolecular forces that govern the interactions between the particles and the walls. Since several mechanisms come into play, it is legitimate to

*Corresponding author: cesare.cejas@espci.fr

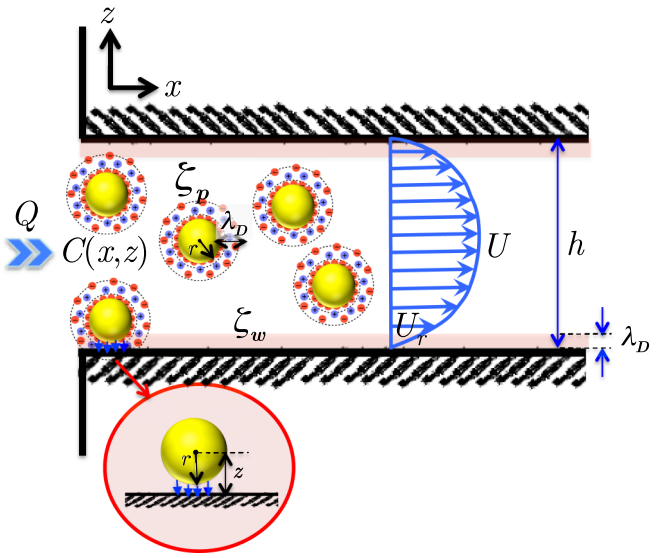

FIG. 1. Scheme showing a concentration of particles, $C(x, z)$, of radius r inside a rectangular channel of height h. Particles and channel walls in aqueous solutions exhibit an electrostatic double layer of length, λ_D, with ζ potentials ζ_w (wall) and ζ_p (particle). Fluid flow follows a parabolic profile with near-wall velocity, U_r, calculated from a Poiseuille profile of average velocity, U_P, and shear effects. The van der Waals adhesion forces act when the particle is within z distance from the wall.

hypothesize that there exist different regimes of deposition, each of them dominated by one particular mechanism and characterized by a specific law. In an n-dimensional diagram, these regimes, along with the surfaces or hypersurfaces that define the transitions between them, could provide the global view of the deposition phenomena that is still lacking in the literature. In a recent work [14], we analyzed one particular regime of deposition, namely, the van der Waals regime, in which the van der Waals forces dominate over electrostatics and diffusion. This work was restricted to high salinities, for which electrostatic forces are screened, and large particles, for which diffusion is negligible. However, in many cases of practical interest, salt concentrations are small or moderate, and particles are Brownian. Moreover, this work [14] did not address the question we raise here, i.e., whether a diagram could represent all the regimes of deposition, thus providing a unified view on the existing numerical and experimental work and, perhaps, inspiring strategies for reducing or enhancing deposition. The present work focuses on figuring out such a diagram for channels of rectangular cross sections. In the present paper, by coupling theory, experiments, and numerics, we succeed to establish it.

II. THEORY

Here we consider a channel of rectangular cross section (Fig. 1) and, for the sake of simplicity, restrict ourselves to the case of shallow channels, i.e., $h \ll w$. We look for stationary fields $C(x, z)$ representing concentrations of particles (i.e., the number of particles per unit of volume) of dilute suspensions, injected at fixed flow rates at the entry of a channel. The rate of injection of the particles in the channel, i.e., the number of injected particles per unit of time, is $\frac{\varphi Q}{v_P}$, where φ is the volumetric concentration of the particles, Q is the flow rate, and v_P is the particle volume. Far from the sidewalls, and in the region $z < \frac{h}{2}$ (for symmetry, we restrict ourselves to this region), $C(x, z)$ is governed by the following mass-conservation equation [17–20]:

$$U_P \frac{\partial C}{\partial x} = \frac{\partial}{\partial x}\left(D\beta_x(z)\frac{\partial C}{\partial x}\right) + \frac{\partial}{\partial z}\left(D\beta_z(z)\frac{\partial C}{\partial z}\right) - \frac{\partial}{\partial z}\left(D\beta_z(z)\left(-\frac{Ar}{6kT(z-r)^2} + \frac{\chi}{\lambda_D}\exp\left(-\frac{z-r}{\lambda_D}\right)\right)C\right), \quad (1)$$

in which $U_P(z) = \gamma(z)U(z)$ (where $U(z)$ is the flow speed is the particle speed and $\gamma(z)$ is given in Appendix A), D is the bulk diffusion coefficient of the particles, $\beta_x(z)$ and $\beta_z(z)$ are dimensionless functions expressing the dependence of the longitudinal and transverse particle diffusion coefficients to the wall with z, k is the Boltzmann constant, T is the temperature, A is the Hamaker constant, λ_D is the Debye length, and r is the particle radius. From the literature, we have $\beta_x(z) = 1 - 9/16z + 1/8z^3 - 45/256z^4 - 1/16z^5$ and $\beta_z(z) = \frac{6(z-r)^2+2r(z-r)}{6(z-r)^2+9r(z-r)+2r^2}$ [21,22]. We also have

$$\chi = 4\pi\epsilon\epsilon_0\zeta_w\zeta_p r, \quad (2)$$

in which ϵ and ϵ_0 are respectively the relative dielectric constant of the fluid transporting the particles and the permittivity of free space, and ζ_w and ζ_p are respectively the zeta potentials of the channel wall and the particle. The left-hand-side term of Eq. (1) is an advective term. On the right-hand side, there are four contributions. The first and second terms represent longitudinal and transverse diffusion, respectively, and the third and fourth terms represent, respectively, the flux of particles driven by van der Waals forces and that driven by electrostatic forces in the Debye layer (in the linear approximation). Here, we restrict ourselves to the case $A > 0$ and negative ζ potentials (repelling case), which represent the experimental situation. Nonetheless, the analysis we carry out here could be extended to the cases where the Hamaker constant is negative and signs of the ζ potentials are different.

We suppose that the concentration is homogeneous at the channel entry $x = 0$ ($C = 1$) and the particles irreversibly adsorb on the walls $z = 0$. Considering particles cannot physically cross the walls and using plane symmetry reasons at $z = \frac{h}{2}$, the boundary conditions (BCs) read [14]

$$x = 0, \quad C = 1; \quad z = r, \quad C = 0; \quad z = \frac{h}{2}, \quad \frac{\partial C}{\partial z} = 0. \quad (3)$$

There is an other approach, equivalent to Eq. (1) and well established in the literature [23–26], that consists in determining the trajectories of each particle by writing that, for each of them, their speed is equal to the forces applied on it times its mobility. This Lagrangian approach provides equations easier to compute, and, in many cases, easier to solve analytically. For the same geometry as above, the Lagrangian equations,

which have the form of a dynamical system, are defined by the following equations (see Appendix B):

$$\dot{x}(t) = \gamma U(z) + \beta_x \delta(t), \tag{4}$$

$$\dot{z}(t) = \beta_z \delta(t) + \frac{d\beta_z}{dz} D + \beta_z \frac{D}{kT}(F_{vdWz} + F_{elz}), \tag{5}$$

in which

$$F_{vdWz} = -\frac{Ar}{6(z-r)^2} \text{ and } F_{elz} = \frac{\chi}{\lambda_D} \exp\left(-\frac{z-r}{\lambda_d}\right). \tag{6}$$

Here x and z are the particle coordinates, and $\delta(t)$ is a zero mean step random function with amplitude $\sqrt{2D\tau}$, where τ is a (supposedly infinitesimal) incremental step. Given the case of shallow channels ($h \ll w$), we assume that the geometry is invariant in the y direction.

For the rest of the paper, we assume continuous injection at rate $\frac{\varphi Q}{v_p}$. In order to work with simple formulas, we introduce a function S defined as [14]

$$S = \left(\frac{\frac{h}{2} - r}{r}\right) \frac{v_p}{\varphi Q t} N_A(t), \tag{7}$$

in which $N_A(t)$ is the number of particles collected by the walls $z = \pm\frac{h}{2}$ as a function of time. The function $\frac{r}{\frac{h}{2}-r} S$ is the collector efficiency, which represents the fraction of the injected particles that are collected by the system. It is an important quantity in engineering literature [27,28]. Thus, our factor S is $\frac{\frac{h}{2}-r}{r}$ times this fraction.

Whenever it is possible, we treat Eqs. (4) and (5) analytically. We also compute them, using a first order discretization in time. The details of the numerical technique are provided in Appendix B.

A. The three regimes of deposition

Since three transport mechanisms control the particle trajectories, namely, diffusion, electrostatics of the Debye layer, and van der Waals forces, we may hypothesize that there exist three fundamental regimes in which one mechanism dominates over the two others and for which, hopefully, explicit expressions for S can be figured out.

Here we analyze these regimes separately.

1. Debye regime

In this regime, the system of Eqs. (4) and (5) reduce to the following equations:

$$\dot{x}(t) = \gamma(z) U(z), \tag{8}$$

$$\dot{z}(t) = \beta_z(z) \frac{D}{kT\lambda_D} \chi \exp\left(-\frac{z-r}{\lambda_d}\right). \tag{9}$$

Equation (9) shows that $\dot{z} > 0$. This implies that, after their injection, particles move away from the wall. Thereby, we have

$$S = 0. \tag{10}$$

Therefore, no particle sticks to the wall in such a regime.

2. van der Waals regimes

These regimes are described by the following equations:

$$\dot{x}(t) = \gamma(z) U(z), \tag{11}$$

$$\dot{z}(t) = -\beta_z(z) \frac{D}{kT} \frac{Ar}{6(z-r)^2}. \tag{12}$$

At this stage, one must distinguish between two situations: in situation or case (i), the collected particles travel far from the wall $z = 0$ (i.e., $z/r \gg 1$, where z is the distance of the centers to the wall, i.e., their altitudes), while in situation or case (ii), they stay close to the wall during their travel, i.e., their centers remain at an altitude $z \approx r$.

(a) van der Waals 1. In this case, as said above, the particles injected in the capture layer travel, in terms of the ratio altitude z over radius, far from the wall. Consequently, β_z and γ are equal to 1, and Eqs. (11) and (12) can be solved analytically. We find

$$S \approx \left(\frac{2A}{3kT} \xi_L\right)^{1/4}, \tag{13}$$

in which

$$\xi_L = \frac{LD}{U_r r^2}, \tag{14}$$

where $U_r = U(r)$. Consequently, the distribution profile along the channel axis (the so-called retention profile, given by the derivative of S with respect to x, with x standing for L) reads

$$p(x) \sim x^{-3/4}. \tag{15}$$

(b) van der Waals 2. This case was analyzed in Ref. [14]. It was shown that, in this regime, the expression for S is

$$S \approx \left(\frac{A}{2.1kT} \xi_L\right)^{1/2}. \tag{16}$$

Consequently, the distribution profile along the channel reads

$$p(x) \sim x^{-1/2}. \tag{17}$$

3. Diffusive regimes

For these regimes, we restrict ourselves to scaling arguments for determining our collection factor S. As particles travel downstream, they move along the streamlines on which they were initially located, but, owing to diffusion, they also move normally to them. In the average, after a time τ, particles initially located on the same streamline move away from it by a distance $\sim\sqrt{D_l \tau}$, where D_l is the local diffusion coefficient. With a local speed U_l, the time τ it takes for the particle to reach the exit of the channel can be estimated by $\frac{L}{U_l}$. Thereby, in the average, particles injected in the channel at a distance $\delta \sim \sqrt{D_l \frac{L}{U_l}}$ from the wall will touch it before they reach the exit and, consequently, be collected. This relation defines the thickness of the "capture layer" δ. By noting that $S \sim \frac{\delta}{r}$ the general expression for S reads

$$S \sim \frac{1}{r} \sqrt{D_l \frac{L}{U_l}}. \tag{18}$$

Now, similarly to the preceding section, one must distinguish between two cases.

(a) Diffusive 1. In this case, the particles wander far from the wall, in terms of the ratio distance over radius. This is precisely the situation addressed by Smoluchowski-Levich [18,20,29]. The expression for S is obtained by replacing D_l by D and U_l by $U_r \frac{\delta}{r}$ in Eq. (18). One obtains

$$S \sim \xi_L^{1/3}. \tag{19}$$

This estimate is consistent with the classical expression of Smoluchowski-Levich [18,20,29], which establishes the transfer rate of particles towards the wall [20,30]. The corresponding distribution of particles along the channel is then

$$p(x) \sim x^{-2/3}. \tag{20}$$

(b) Diffusive 2. In this case, the particles remain at an altitude $z \approx r$ during their travel along the channel. By replacing D_l by $D\frac{\delta}{r}$ and U_l by U_r (in a way similar to case (i) of the van der Waals regime), one obtains

$$S \sim \xi_L. \tag{21}$$

The distribution profile along the channel is given by

$$p(x) \sim \text{Cst}. \tag{22}$$

Note that in the diffusive 1 regime, we have $\delta \gg r$, while in the diffusive 2 regime, since the particles travel close to the wall, the capture layer thickness δ should be considered much smaller than r. This implies that in the former case, $S \sim \frac{\delta}{r} \gg 1$ while in the latter, $S \ll 1$.

The four subregimes discussed above have been studied numerically, in some detail (see Appendix C). Figures 8 and 9 (in Appendix C) show that the scaling laws we establish here agree well with the numerics. Their prefactors could moreover be calculated. For the diffusive 1 regime, we found

$$S \approx 0.8\xi_L^{1/3}. \tag{23}$$

For the diffusive 2 regime, we obtained

$$S \approx 0.5\xi_L. \tag{24}$$

For the other regimes, the theoretical prefactors agreed well with the numerics.

The four subregimes can be represented in the diagram shown in Fig. 2, using ξ_L and $\frac{A}{kT}$ as coordinates. In such a diagram, each frontier is determined by writing that, at the boundaries between two regimes, the values of S match. The corresponding equations of the frontiers $\xi_L = f(\frac{A}{kT})$ are indicated in the caption of Fig. 2. The diagram of Fig. 2 has been well confirmed numerically (see Fig. 9 in Appendix C). An earlier work [14] focusing on van der Waals 2 is in agreement with regards to its position in Fig. 2.

B. The transition between Debye and van der Waals regimes

The region, in the parameter space, where Debye and van der Waals forces both play a role, is governed by the following equations:

$$\dot{x}(t) = \gamma U(z), \tag{25}$$

$$\dot{z}(t) = \beta_z \frac{D}{kT}\left(-\frac{Ar}{6(z-r)^2} + \frac{\chi}{\lambda_D}\exp\left(-\frac{z-r}{\lambda_D}\right)\right). \tag{26}$$

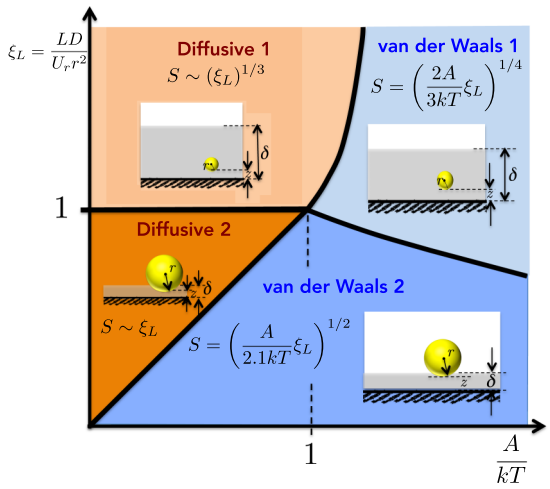

FIG. 2. Phase diagram of the four subregimes: (i) diffusive 1, where $S \sim \xi_L^{1/3}$; (ii) diffusive 2, where $S \sim \xi_L$; (iii) van der Waals 1, where $S = (\frac{2A}{3kT}\xi_L)^{1/4}$; and (iv) van der Waals 2, where $S = (\frac{A}{2.1kT}\xi_L)^{1/2}$. The frontier between diffusive 1 and diffusive 2 is $\xi_L = 1$. The frontier between diffusive 1 and van der Waals 1 is $\xi_L \sim (\frac{A}{kT})^3$. The frontier between diffusive 2 and van der Waals 2 is $\xi_L \sim \frac{A}{kT}$. The frontier between van der Waals 1 and van der Waals 2 is $\xi_L \sim (\frac{A}{kT})^{-1}$.

By introducing the variables $\eta = \frac{(z-r)}{\lambda_D}$ and $t' = t\frac{D}{kT}\frac{\chi}{\lambda_D^2}$, one obtains an adimensionalized form of Eq. (25):

$$\frac{\dot{\eta}(t')}{\beta_z(\eta)} = F(\eta) = -\frac{P}{\eta^2} + \exp(-\eta), \tag{27}$$

in which we have

$$P = \frac{Ar}{6\chi\lambda_D}. \tag{28}$$

The behavior of the system, i.e., whether particles are attracted or repelled by the wall, is controlled by the sign of $\dot{\eta}(t')$, which, in turn, is controlled by $F(\eta)$. The shape of $F(\eta)$ is sketched in Fig. 3. Two possibilities exist:

(i) $P > P_C = 4\exp(-2)$. In this regime, the function $F(\eta)$ is always negative. Thus, in this case, similarly as in the van der Waals regimes, there exists a "force" that drives the particles towards the wall, favoring their collection.

(ii) $P < P_C = 4\exp(-2)$. The force is positive within a range of values of η, defined by the roots η_1, η_2 of the following equation:

$$\eta^2\exp(-\eta) = P. \tag{29}$$

One root (η_1) is smaller than $\eta_C = 2$, while the other (η_2) is larger than $\eta_C = 2$. Above the larger root, the "force" $F(\eta)$ is attractive, and consequently particles initially injected at $\eta > \eta_2$ start moving towards the wall as they travel downstream. However, for $\eta < \eta_2$, F changes sign and particles are repelled. Therefore, they accumulate at the location $\eta = \eta_2$, and exit the channel without being collected. Particles injected at $\eta_1 < \eta < \eta_2$ undergo the same process. Only those injected at $\eta < \eta_1$ are attracted towards the wall. If we assume (owing to their proximity to the wall) that all are collected, the factor

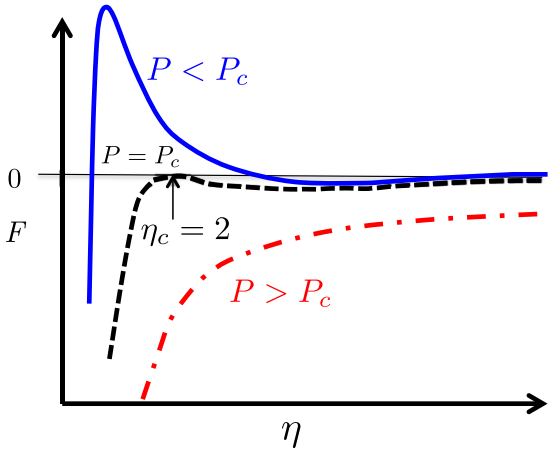

FIG. 3. Sketch of $F(\eta)$ [Eq. (27)] as a function on η based on numerical simulation results. The condition $P > P_C$ (dash-dotted red line), where $P_C = 4\exp(-2)$, demonstrates a negative force resulting in attractive interaction between two surfaces. The condition $P < P_C$ (solid blue line) demonstrates a positive force within a range of η. Finally, the condition $P = P_C$ (dashed black line) represents a critical case between two regimes.

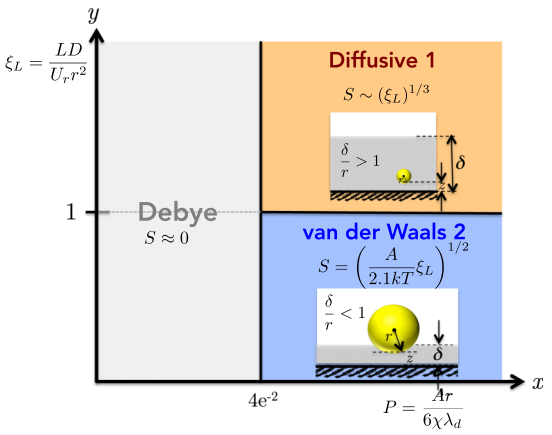

FIG. 4. The universal diagram of particle deposition represented as ξ_L [Eq. (14)] in the y axis as a function of dimensionless number P [Eq. (28)] in the x axis. The transition from diffusive 1 to van der Waals 2 is marked by $\xi_L \sim 1$ and that from Debye to diffusive 1 or van der Waals 2 corresponds to $P = 4e^{-2}$.

S can be estimated by the expression

$$S \approx \eta_1 \frac{\lambda_D}{r}. \tag{30}$$

To summarize, when $P > P_C = 4\exp(-2)$, particles are collected in a manner similar to van der Waals regimes, while, when $P < P_C = 4\exp(-2)$, particles split into two subpopulations, one concentrated along the line $\eta = \eta_2$ and the other collected at the channel wall. Because of the presence of a barrier, one may expect that the quantity of particles collected at the wall is much larger when $P > P_C$ than in the opposite case. The equality $P = P_C$ thus represents a frontier between a regime where van der Waals forces dominate, favoring collection, and another one where electrostatic forces prevail, preventing collection. We take this equality to define the boundary between the van der Waals and Debye regimes.

C. The transition between Debye and diffusive regimes

Figure 3 can be also used to discuss the transition between Debye and diffusive regimes, in a manner similar to the stability of colloidal suspensions, based on DLVO theory [11]. When $P < P_C$, most particles do not approach the wall because of a barrier located at $P = P_C$. Still, owing to Brownian motion, a few of them can cross this barrier and deposit on the wall if their thermal "force" has an intensity comparable to or larger than the barrier height. When $P \leqslant P_C$, the barrier collapses and thermal fluctuations can drive all the particles towards the wall without being blocked by electrostatic forces. The flux towards the wall will thus be much more abundant. This reasoning indicates that $P = P_C$ represents a frontier between a regime dominated by electrostatic repelling forces and another dominated by thermal fluctuations. As above, we take the condition $P = P_C$ to define the boundary between the Debye and diffusive regimes. Remarkably, this frontier is located at the same position as that separating the Debye from the van der Waals regimes.

D. Universal diagram for $\frac{A}{kT} \sim 1$

The preceding results can be summarized in Fig. 4, which shows the range of existence of the various regimes as a function of ξ_L [Eq. (14)] and P [Eq. (28)].

As explained below, in our experiments, with the materials we use [PS beads and hydrophobic polydimethylsiloxane (PDMS)] we work at a fixed value of $A/kT \approx 2$. Therefore, as we change the parameters of the experiment, the system evolves along a vertical line of Fig. 4, that essentially crosses the van der Waals 2 and diffusive 1 regimes, the transition taking place at $\xi_L \sim 1$. The other subregimes (van der Waals 1 and diffusive 2), which are difficult to access experimentally with the materials currently used in microfluidics, are not investigated in the present paper.

To establish the diagram of Fig. 4, we thus restricted ourselves to $\frac{A}{kT} \sim 1$. Consequently, only one diffusive (diffusive 1) and one van der Waals regime (van der Waals 2) appear on Fig. 4.

This diagram takes the form of a cantilever beam, with a vertical support located at $P = 4\exp(-2)$ and a horizontal bar located at $\xi_L \approx 1$. It is interesting to note that, according to the theoretical results of the preceding sections and the remark made above on the value of the ratio δ/r, each regime is associated to the following conditions on S:

(i) The van der Waals regime is associated to $\frac{S}{S_{vdW}} \approx 1$ (in which $S_{vdW} = (\frac{A}{2.1kT}\xi_L)^{1/2}$) and $S = \delta/r < 1$.

(ii) The diffusive regime is associated to $\frac{S}{S_{\text{diff}}} \approx 1$ (in which $S_{\text{diff}} \approx 0.8\xi_L^{1/3}$) and $S = \delta/r > 1$.

(iii) The Debye regime is associated to $S \approx 0$.

These relations will serve as criteria to determine, without *a priori* knowledge, to which regime a particular set of flow conditions belongs. In practice, to identify the regime, we measure S and determine in which of the three above intervals

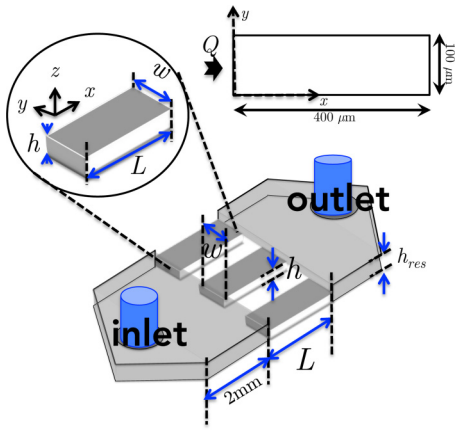

FIG. 5. Scheme of the PDMS-based microfluidic chip consisting of parallel rectangular channels, of dimension hwL. The channels are flanked by inlet and outlet reservoirs of height h_{res}. The channels are 150 μm apart to avoid cake formation so each channel acts independently from one another.

the quantity lies, taking the experimental uncertainty into account.

III. EXPERIMENTAL RESULTS AND DISCUSSION

A. Experimental setup

The experimental setup is shown in Fig. 5. We use a microfluidic chip to experimentally investigate the different deposition regimes with microchannels having dimensions of 400 μm (L), 10 and 20 μm (h), and 100 μm (w) between entry and exit reservoirs. The total length of the chip is about 2 mm, including the entry and exit reservoirs. The reservoirs have a height $h_{\text{res}} \sim 30$ μm. The chip actually consists of a series of parallel rectangular channels. The channels are 150 μm apart to avoid cake formation that could disrupt flow. At this distance, each channel acts independently from one another. The chips are made from silicon wafer molds, fabricated using standard soft lithography techniques. The chips are made of PDMS using a 10:1 polymer:cross-linker ratio. The polymer solution is commercial grade Sylgard 184 silicon elastomer base (Dow Corning GmbH, Germany) while the cross-linker is Sylgard 184 silicon elastomer curing agent (Dow Corning GmbH, Germany). Once prepared, the polymer solution was then poured into the silicon wafer mold and the solution was degassed to remove bubbles. Once the bubbles were removed, the mold was transferred to an oven at 65°C. Once the PDMS solution had hardened, the cured PDMS was peeled off the silicon wafer mold. The chips were cut to shape and punched with holes for inlet and outlet tubes. Using plasma treatment, the chips were then bonded onto PDMS-coated glass slides. The plasma treatment induces siloxane bonds, temporarily rendering the PDMS hydrophilic. After about 2–3 h, the PDMS returned to its hydrophobic condition. We used a Veeco optical profilometer to characterize the surface roughness of PDMS substrates. A typical channel has a root-mean-squared average roughness of $R_q = 3.12$ nm.

Colloidal particles are transported onto the channel by a pressure difference set by a pressure controller (Fluigent). The glass slide upon which the PDMS structure is attached is spin-coated with PDMS. We keep the surface treatments of the channel walls hydrophobic (device heated at 95°C for at least 4–5 h). We determine the flow rate Q by measuring average particle speeds, from a fixed distance from the channel entry. We perform experiments at low Reynolds numbers (Re $\sim$ 0.03–0.89). We vary parameters such as U, L, φ, and h by at least one order of magnitude. The suspensions are dilute, with concentrations (w/v) ranging between 0.003% and 0.3%. The salt concentrations range from $10^{-4}M$ to $1M$ NaCl, i.e., over four orders of magnitude.

We use different commercial particles: in a first series of experiments, particularly for the van der Waals regime, we use monodisperse PS microparticles (Sigma-Aldrich) with diameter $d = 5$ μm. The micrometric particles are density matched with water so they do not sediment during the experimental observation window. In addition, the particles have different refractive indices than water and this refractive index mismatch permits contrast and facile observation of the deposited particles on the wall. These particles are unfunctionalized, though they are negatively charged due to remaining initiator fragments after polymerization [31]. The Hamaker constant, A, for these particles on PDMS surfaces in saline aqueous suspension was determined to be $A = 8 \times 10^{-21}$ J [14] (and therefore $\frac{A}{kT} \approx 2$). In the literature, comparison with Lifshitz or pairwise additivity theory often suggests that the Hamaker constant can vary, by several tens of percent [11,20,32–35] with the salt concentration. Although, some studies [36] have pointed out that for certain materials the Hamaker constant is ultimately independent of electrolyte concentration. For simplicity, we take the same constant for all the concentrations we consider, whenever it is needed for interpreting the measurements.

In another series of experiments, particularly for the diffusive regime, we use colloidal nanoparticles of diameter $d = 500$ nm. The nanoparticles are carboxylated functionalized polystyrene particles (Thermo Fisher Scientific) and are fluorescent for increased visibility. Theory [32,37,38] suggests that, with the presence of a surface layer, the Hamaker constant characterizing the wall and functionalized particles slightly changes in comparison with the naked particle. Comparison with literature [37,38] shows that at relatively large particle-wall separations, the vdW interactions are dominated by the property of the bulk particle and not by the surface modification. For simplicity, we neglect such a change and also take $A = 8 \times 10^{-21}$ J for the Hamaker constant for these polystyrene-based particles, whenever the Hamaker constant is needed for interpreting the measurements.

Salt concentrations were prepared by dissolving the appropriate quantity of sodium chloride, NaCl (ReagentPlus $\geqslant$ 99.5%, Sigma Aldrich) in a specific volume of deionized water. The salt concentrations prepared ranged from $0.0001M$ to $1M$ salt. The pH was also tested especially for high salt concentrations and the pH remained approximately constant at pH $\sim$ 6.5. When the suspending fluid contains substantial concentrations of salt, the suspension stability is problematic, especially for nanoparticles. To avoid clustering, we sonicated the suspensions for about 45–60 min before experiments and our solutions were dilute enough to minimize interparticle aggregation. Nevertheless, in order to control the absence

of aggregation during the time the particles travel in the device, we collected the suspension at the outlet of the device and performed dynamic light scattering (DLS) measurements (Malvern Zetasizer Instruments; see SI-1 in the Supplemental Material [39]). The results were compared to the size given by the commercial company, and to DLS measurements performed prior to the injection, after sonication within the same duration. Results showed that, at the maximum salinity ($1M$ NaCl) using dilute particle concentrations, 80% of the particles have not aggregated. We conclude that clustering is negligible.

The use of fluorescence in the visualization of smaller particles means that some experiments can be subject to photobleaching, which is described as a reduction in fluorescence emission intensity [40,41]. This could have an influence on particle count and visualization especially if particles can no longer be easily detected during image treatment. We performed a photobleaching curve correction on the pixel-intensity values to recover lost signals and increase detection. With the use of 500-nm particles, high aperture objectives are needed and it is difficult to simultaneously observe both the bottom (floor) and top (ceiling) of the channel in the z direction, even at $40\times$ magnification. Thus, images of adsorbed particles only show one side of the channel. To verify the symmetry of particle deposition, i.e., an approximately equal number of adsorbed particles in both the floor and ceiling of the channel, we perform experiments where, in the course of the flow, we change the focus from the floor to the ceiling. Results (see SI-2 in the Supplemental Material [39]) show symmetric deposition in both floor and ceiling and we take this symmetry factor into account when determining the total number of adsorbed particles. It should be noted that with particles $d = 5\ \mu$m and $h = 20\ \mu$m, because objectives of lower numerical aperture are used, sticking events can be observed simultaneously in both the floor and ceiling of the channel. But it is not the case with the 500-nm particles.

We use Leica or Zeiss optical microscopes for observing fluid flow and particle deposition, injected by pressure difference set by a pressure controller (Fluigent). Cameras used in data acquisition include RD Vision and Photron Fastcam SA3, which are connected to the optical microscopes. Throughout the studies, we harness the advantages of microfluidics by performing multiple experimental runs for each case, thereby improving statistics. Each experiment is repeated a minimum of three times to ensure reproducibility. In every experiment, we use MATLAB R2016 image treatment. We eliminate all other particles that are advected across the channel and extract the particles that have been deposited on the walls. We use standard image analysis techniques, such as histogram equalization and binarization to enhance the contrast between the wall and the deposited particles. We then analyze individual single-particle deposition events by measuring the following quantities: (1) histogram of the particle sticking lengths, $p(x)$, defined as the distance between the deposited particles and the channel entrance; and (2) the number of particles adsorbed as a function of time, $N_A(t)$, in the first few seconds of deposition, where particle deposition occurs on naked surfaces. At much later times, the surface is substantially filled with particles, and $N_A(t)$ starts leveling off [14]. We do not consider such a regime.

B. The universal diagram for $A/kT \approx 2$

Figure 6 shows typical examples of the measurements we perform. The three experiments shown in Fig. 6 are performed in the similar channels with identical flow rates, but with different particle sizes and salt concentrations. Figures 6(a1)–6(c1) show typical images of the three deposition regimes at similar temporal observation windows. Figure 6(a2)–6(c2) show measurements of $N_A(t)$ for these flow conditions, along with the corresponding retention profiles in Figs. 6(a3)–6(c3).

In order to figure out which regime each set of experimental conditions belongs to, we need to calculate S in each case and apply the criteria defined in Sec. II D. Here, we assume that the experiment only explores diffusive 1, van der Waals 2, and Debye regimes. Under this hypothesis, the problem we have to solve is to determine to which of these three regimes a particular set of conditions belongs to.

In Figs. 6(a4)–6(c4) we have plotted S as a function of time. For reading convenience, we recall here the definition of S [initially shown in Eq. (7)]:

$$S = \left(\frac{\frac{h}{2} - r}{r}\right)\frac{v_p}{\varphi Q t}N_A(t). \tag{31}$$

In all cases, S is independent of time, which is logical, because we found $N_A(t)$ proportional to time. In Fig. 6(a4), we see that S is smaller than 1. Moreover, S is indistinguishable from the theoretical prediction for the van der Waals 2 regime $S = (\frac{A}{2.1kT}\xi_L)^{1/2} \approx 0.09$. Criterion (i) introduced previously (see Sec. II D) being satisfied, we can conclude that this set of experimental conditions falls into the van der Waals 2 regime. A similar reasoning applied to Fig. 6(b4) leads to the conclusions that we are in the diffusive 1 regime, because S is both larger than unity and in good agreement with the expected value for the diffusive 1 regime. In Fig. 6(c4), the value of S is below unity and moreover much smaller than the van der Waals 2 regime, which would lead to $S \approx 0.09$; therefore, the only possibility is that we are in the Debye regime.

Once the regimes or subregimes are identified, it becomes permissible to compare the theoretical retention profiles with the experimental measurements. This is done in Figs. 6(a3)–6(c3). We obtain that, whenever the number of particles is sufficient to establish a distribution profile, the theory agrees well with the measurements.

By applying the same methodology to all the measurements we made, we can establish a universal diagram, using the variables of the theory, i.e., ξ_L [Eq. (14)] and P [Eq. (28)]. Both are known experimentally since all quantities included in their definitions are known or measurable. This leads to Fig. 7(a). A particular symbol is attributed to each regime. One can see that the experiment (solid symbols) agrees remarkably well with the theoretical predictions, the agreement having been obtained throughout six orders of magnitude on the horizontal axis and eight on the vertical axis. Numerics (open symbols), in which we used the same criteria as the experiments to define the various regimes, provides an additional support to the theory.

For practical reasons, we represent the experimental data in another manner. Figure 7(b) uses the salt concentration instead of parameter P. Here, the universal diagram is presented in

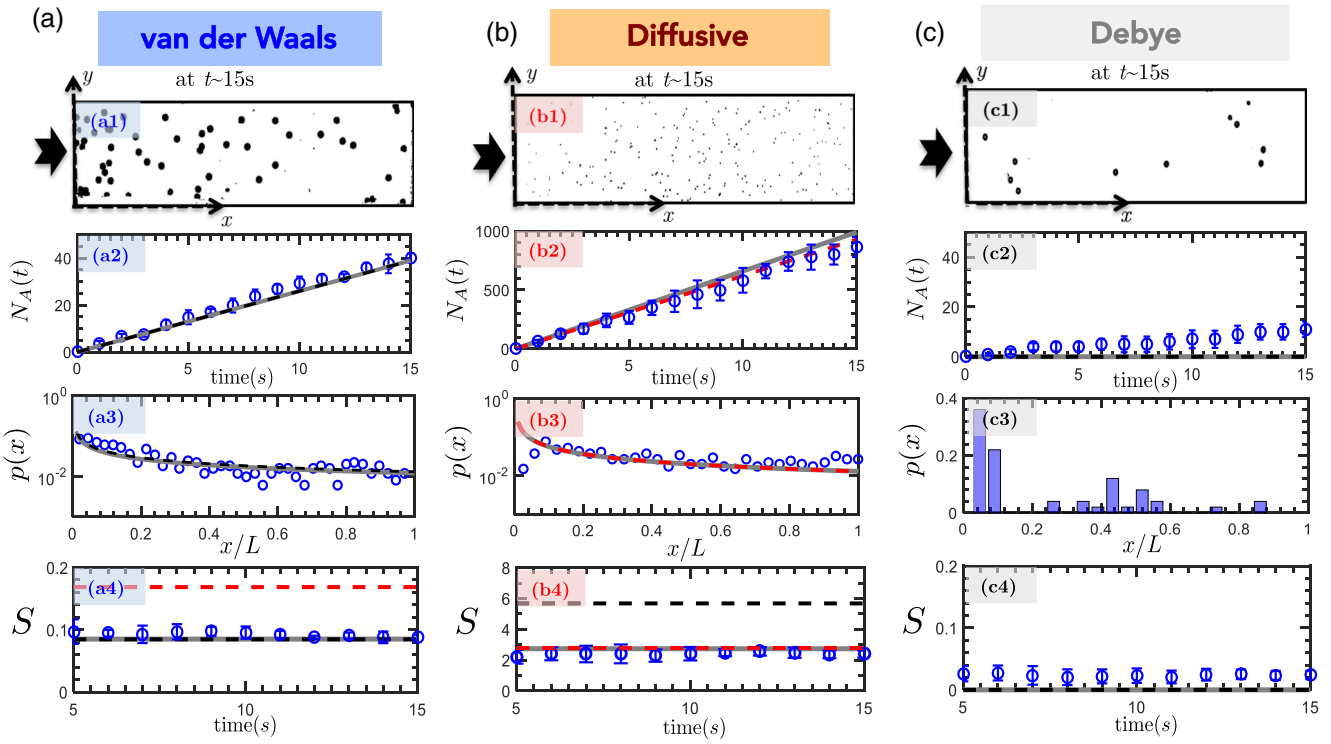

FIG. 6. Experimental results of different deposition regimes. Error bars reflect 95% confidence levels. In all cases, black broken lines represent respective theoretical expressions while solid grey lines represent numerical simulation results performed under the same conditions as the experiments. (a1) van der Waals 2 (vdW) regime showing deposited microparticles at $\xi_L = 0.0078$, $1M$ NaCl $d = 5\ \mu$m, $h = 20\ \mu$m, $w = 100\ \mu$m, $L = 400\ \mu$m, $U = 1$ mm/s, $\varphi = 0.3\%$, and $A = 8 \times 10^{-21}$ J [14]. Images have been treated to show immobile particles as black spots (a2) $N_A(t)$ for PS-hydrophobic PDMS, where data follow S_{vdW} [Eq. (16)]. (a3) Histogram distribution (normalized density in semilogarithmic format), showing deposited particles in both channel floor and ceiling, where data follow $y \sim x^{-1/2}$ [Eq. (17)]. (a4) Plot of $S(t)$ [Eq. (31)] for vdW, where $S \approx 0.09$ ($S < 1$), compared with S_{vdW} [black broken line, Eq. (16)] and S_{diff} [red broken line, Eq. (23)]. (b1) Diffusive 1 (diff) regime showing deposited nanoparticles at $\xi_L \sim 35.06$, $1M$ NaCl, $d = 0.5\ \mu$m, $h = 10\ \mu$m, $w = 100\ \mu$m, $L = 400\ \mu$m, $U = 1$ mm/s, $\varphi = 0.003\%$, $A = 8 \times 10^{-21}$. (b2) $N_A(t)$ for carboxylated PS-hydrophobic PDMS, where data follow S_{diff} [Eq. (23)]. (b3) Histogram distribution (in semilogarithmic format), where data only show particles deposited on the floor (see Supplemental Material SI-2 [39]). The data follow $y \sim x^{-2/3}$ [Eq. (20)]. (b4) $S(t)$ [Eq. (31)] for diffusive, where $S \approx 2.7$ ($S > 1$), compared with S_{diff} [red broken line, Eq. (23)] and S_{vdW} [black broken line, Eq. (16)]. (c1) Debye regime showing deposited microparticles on both the floor and the ceiling at $\xi_L = 0.0078$, $d = 5\ \mu$m, $h = 20\ \mu$m, $w = 100\ \mu$m, $L = 400\ \mu$m, $U = 1$ mm/s, $\varphi = 0.3\%$ at $0.007M$ NaCl. (c2) $N_A(t)$ for PS-hydrophobic PDMS at 0.007M NaCl. (c3) Histogram distribution at $\xi_L = 0.0078$ at the end of the experiment. Results show sporadic profiles with few deposited particles. (c4) $S(t)$ [Eq. (31)] for Debye regime where the theoretical expectation is $S = 0$ [black broken line, Eq. (10)].

three dimensions using C_{salt} in mol/L (x axis), ξ_L (y axis), and S/S_{vdW} (z axis), the latter quantities being chosen for obtaining a clear representation. Like in Fig. 6, we obtain an excellent agreement between the theoretical expectations, the numerics, and the experiment. Figure 7(c), which represents cuts of the three-dimensional (3D) diagram along two different planes, further confirms the agreement. The 3D diagram of Fig. 7(b) thus provides a general picture of the regimes of deposition taking place in the system we study. Compared to Fig. 6, Fig. 7 also provides estimates of the number of particles that are collected to the walls. In Fig. 7, it is interesting to note that the cross-over between the Debye regime and the other regimes takes place at a salt concentration on the order of $0.1M$. This corresponds to the common wisdom that, above this order of magnitude, electrostatic (repulsive) charges are screened and particles tend to be captured by the walls. Here, we provide an explanation for this empirical fact, by noting that it reflects the critical condition $P_C = 4\exp(-2)$, which, in practice, for many fluid-particle systems, effectively leads to critical concentrations on the order of $0.1M$.

IV. CONCLUSION

Based on experiments using shallow microchannels of rectangular cross sections, and with the support of numerical simulations and theory, we explain quantitatively the deposition kinetics of individual colloidal particles, along with their corresponding retention profiles. The model reproduces the experimental observations remarkably well, within a broad range of geometrical, flow, or concentration parameters. This extends our previous work [14], which addressed a particular regime of deposition and did not raise the question of the existence of a universal diagram providing a global vision on deposition phenomena in microchannels.

In the present work, we thus succeeded to establish a universal diagram of particle deposition, thus far lacking in the

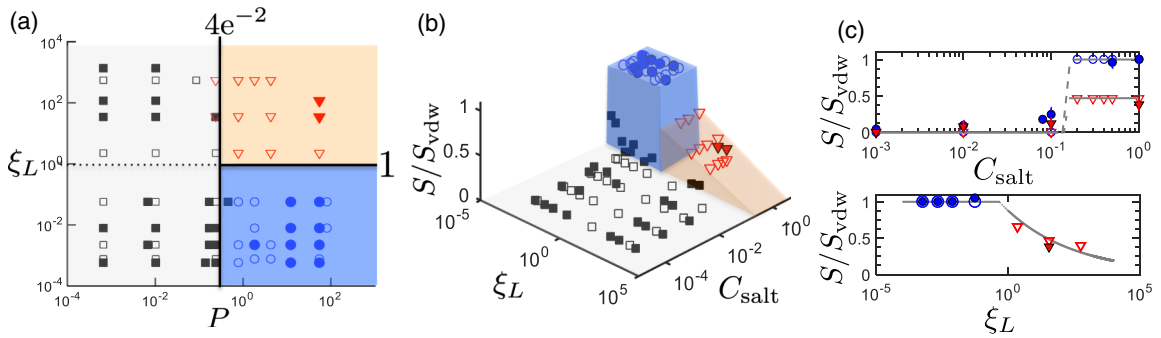

FIG. 7. (a) Universal diagram of particle deposition with both experimental and numerical results presented as ξ_L [Eq. (14)], as a function of P [Eq. (28)], as defined by the two-dimensional (2D) theoretical diagram in Fig. 4. In two dimensions, the vertical line is defined by $P = 4e^{-2}$, and the horizontal line in terms of $\xi_L = 1$. In all cases, solid symbols represent experimental points while open symbols are numerics. (b) The universal diagram presented in practical or operational terms in three dimensions with the deposition ratio S/S_{vdW} as a function of C_{salt} (salt concentration in M) and ξ_L. The parameter C_{salt} can be extracted from the parameter P [Eq. (28)]. Note that the vdW regime is associated with $\xi_L < 1$ while the diffusive regime is associated with $\xi_L > 1$. (c, top) Slice of the plane along S/S_{vdW} as function of C_{salt}, showing the transitions from Debye to van der Waals (blue) and Debye to diffusive (red). Grey lines are theoretical predictions and the grey dashed line is drawn to guide the eye. (c, bottom) Slice of the plane along S/S_{vdW} as function of ξ_L showing $S/S_{vdW} \approx 1$ in the vdW regime while showing $S/S_{vdW} \approx \xi_L^{-1/6}$ in the diffusive regime. Legend: Circles and inverted triangles denote the Debye regime, where numerics and experiments are performed with these parameters: $h = 20\ \mu$m, $w = 100\ \mu$m, $L = 400\ \mu$m, $\varphi = 0.3\%$, while varying U, r, and relative low C_{salt} ($10^{-4}M$–$10^{-1}M$ NaCl). Inverted red triangle denote the diffusive regime, where numerics and experiments are performed with these parameters: $h = 10\ \mu$m, $w = 100\ \mu$m, $L = 400\ \mu$m, $\varphi = 0.003\%$, while varying U, r, and at relatively high C_{salt} ($0.1M$–$1M$ NaCl). Blue circles denote the van der Waals regime, where numerics and experiments are performed with these parameters: $h = 20\ \mu$m, $w = 100\ \mu$m, $L = 400\ \mu$m, $\varphi = 0.3\%$, $A = 8 \times 10^{-21}$ J, while varying U, r, and relative high C_{salt} ($0.1M$–$1M$ NaCl).

literature. This diagram could prove a useful guide in not just predicting deposition behavior, but also in adapting different physical parameters for various targeted applications. The advantage of the universal diagram is that it provides a paradigm to fine-tune physical parameters to allow one condition to dominate over the other. This will be most useful to design systems dedicated to favor or reduce particle deposition, depending on the application. Also, the present analysis provides explanations for empirical observations left without precise explanation, such as the critical salt concentrations above which deposition becomes important, and, apart from a particular range of conditions (difficult to achieve experimentally), the systematic abundance of particles close to the injection inlets in microchannels, which should not be interpreted as a vague entry effect, but rather as a consequence of the kinetics of the deposition process.

ACKNOWLEDGMENTS

This work has been supported by ESPCI Paris - IPGG (program ANR-10-EQPX-34), and Sanofi. We also thank CNRS Gulliver UMR 7083 and the Microfluidics, MEMS, Nanostructures (MMN) group. We also thank Loic Saulin for the 3D plot as well as scientific discussions with Lydéric Bocquet.

C.M.C. developed and performed experiments as well as automation of the MATLAB image treatment code and also performed numerical simulations; F.M. helped in experimental design setup; M.T. provided assistance in image analysis coding particularly in separating the particles that stick and those that do not stick; J.P.B. provided consultation and financing; P.T. developed theoretical analysis and the numerical simulation code; and C.M.C. and P.T. both wrote the manuscript.

APPENDIX A: CALCULATIONS FOR $\gamma(\eta) = \frac{U_P}{U_r}$

The particle speed U_p has been calculated by Refs. [21,22]. By introducing the ratio

$$\gamma(\eta) = \frac{U_p(r)}{U_r}, \tag{A1}$$

where $U_r = \frac{6Qr}{wh^2}(1 - \frac{r}{h})$ is the flow speed at $z = r$, $\gamma(\eta)$ has the following expression, and $\eta(z) = \frac{z-r}{r}$. For $\eta > 1$,

$$\gamma(\eta) = 1 - \frac{5}{16\eta^3}, \tag{A2}$$

for $10^{-4} < \eta < 1$,

$$\gamma(\eta) = \frac{1}{\eta + 1}\exp(0.68902 + \log(\eta) + 0.072332\log^2(\eta) + 0.0037644\log^3(\eta)), \tag{A3}$$

and for $\eta < 10^{-4}$,

$$\gamma(\eta) = \frac{0.7431}{0.6376 - 0.2\log(\eta)}. \tag{A4}$$

APPENDIX B: NUMERICAL SIMULATIONS

To establish Eqs. (4) and (5) in the main text, we use Langevin equations of the general form [4,12,13,17]

$$\dot{\mathbf{r}}_i(t) = \frac{\mathbf{D}_i\mathbf{F}_i}{kT} + \nabla\cdot\mathbf{D}_i + \mathbf{U}(\dot{\mathbf{r}}_i) + \Delta(t), \tag{B1}$$

where $\dot{\mathbf{r}}_i$ is the vector position of the ith particle, $\mathbf{D}_i$ is the anisotropic diffusion, $\mathbf{F}_i$ is the total force acting on the particle, and $\mathbf{U}$ is the contribution of the flow to the particle speed. In simple geometries, such as the one we consider (straight channel), these quantities are documented and their

expressions are available in the literature. $\Delta(t)$ is the random Brownian displacement.

By applying these general equations to the particular geometry we consider, i.e., long shallow channels with rectangular cross sections, we obtain the following equations:

$$\dot{x}(t) = \gamma(z)U(z) + \beta_x(z)\delta(t), \tag{B2}$$

$$\dot{z}(t) = \beta_z(z)\delta(t) + \frac{d\beta_z}{dz}D + \beta_z\frac{D}{kT}(F_{vdWz} + F_{elz}), \tag{B3}$$

in which

$$F_{vdWz} = -\frac{Ar}{6(z-r)^2} \text{ and } F_{elz} = \frac{\chi}{\lambda_D}\exp\left(-\frac{z-r}{\lambda_d}\right), \tag{B4}$$

where $\gamma(z)$ is given in Appendix A, $\beta_z(z) = \frac{6(z-r)^2+2r(z-r)}{6(z-r)^2+9r(z-r)+2r^2}$, and $\beta_x(z) = 1 - 9/16z + 1/8z^3 - 45/256z^4 - 1/16z^5$ [21,22].

Considering the numerical method used to compute Eqs. (4) and (5), we proceed similarly as in Refs. [12,14,42,43]. The code is provided in the Supplemental Material (see SI-3 [39]). The time derivatives are replaced by a first order discretization. Although, ideally, τ (simulation time step) should be as small as possible, in practice, taking a τ too small leads to large computing times. In practice, the values we take for τ range between 0.5×10^{-6} and 1.5×10^{-5}. In all cases, these values are well below the characteristic times of the problem and we checked that the results are insensitive to the particular value of τ taken within this range. For the boundary conditions, we impose that, if the particles are below some distance away from the wall, they irreversibly stick on the wall (we perform additional checks and determine that the choice of this distance—in the range 0.1–1 nm—is not critical) [14]. We consider channel symmetry at $z = h/2$ and $y = w/2$ and only count the individual singular particles adsorbed on floor and ceiling.

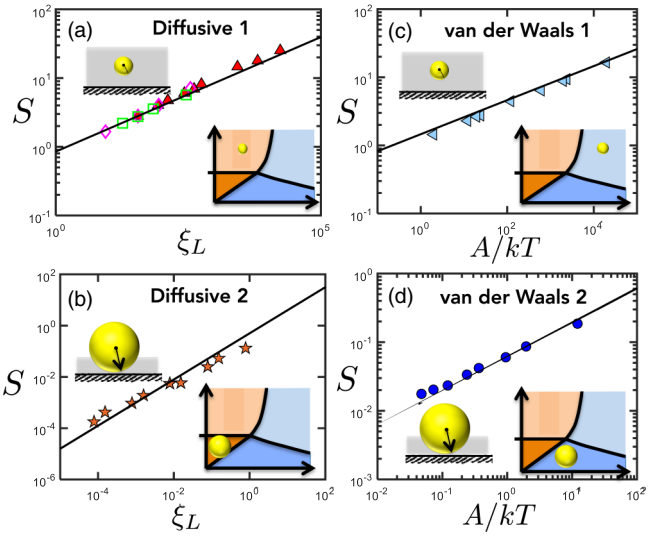

FIG. 8. Numerical checks of the theoretical predictions for the four subregimes discussed in preceding sections: (a) diffusive 1, (b) diffusive 2, (c) van der Waals 1, and (d) van der Waals 2. Solid lines in all four graphs correspond to theoretical predictions, while inset sketches show the position of the subregime with respect to the diagram shown in Fig. 2. Legend: (a) ▲, $h = 20$ μm, $\varphi = 0.3\%$, $L = 400$ μm, $A = 8 \times 10^{-21}$ J, $U = 1$ mm/s, $0.1 \leqslant r \leqslant 0.5$ μm; ◇, $h = 20$ μm, $\varphi = 0.3\%$, $A = 8 \times 10^{-21}$ J, $U = 1$ mm/s, $r = 0.25$ μm, 40 μm $\leqslant L \leqslant 10$ cm; □, $\varphi = 0.3\%$, $L = 400$ μm, $A = 8 \times 10^{-21}$ J, $U = 1$ mm/s, $r = 0.25$ μm, 5 μm $\leqslant h \leqslant 1$ mm. (b) ⬟, $h = 20$ μm, $\varphi = 0.3\%$, $A = 1 \times 10^{-24}$ J, $r = 2.5$ μm, $0.001 \leqslant U \leqslant 100$ mm/s. (c) ◁, $h = 20$ μm, $\varphi = 0.3\%$, $L = 400$ μm, $1 \times 10^{-21} \leqslant A \leqslant 8 \times 10^{-17}$ J, $U = 1$ mm/s, $r = 0.25$ μm, $\xi_L = 6.8$. (d) ●, $h = 20$ μm, $\varphi = 0.3\%$, $L = 400$ μm, $2 \times 10^{-22} \leqslant A \leqslant 5 \times 10^{-20}$ J, $U = 1$ mm/s, $r = 2.5$ μm, $\xi_L = 0.0078$.

APPENDIX C: NUMERICAL CHECK OF THE THEORY

To compare theory and numerics, we perform numerical simulations for a range of varying A/kT ratios, L, U, h, and r:

(i) In the vdW 1 regime, where the capture layer $\delta > r$, we use a fixed value of U and relatively small r such that $\xi_L > 1$.

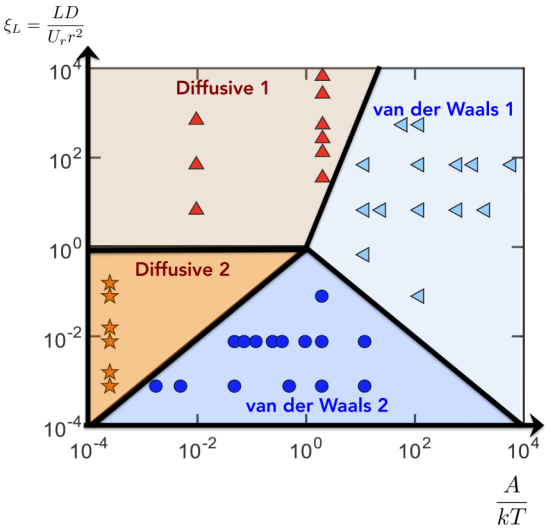

FIG. 9. Numerical checks of the theoretical predictions for the four subregimes showing $\xi_L(\frac{A}{kT})$. Solid lines correspond to theoretical expressions of the frontiers (see Fig. 2 caption), while symbols are different numerical simulation results. Common parameters for these simulations include $h = 20$ μm, $\varphi = 0.3\%$, and $L = 400$ μm. Certain other parameters vary with respect to the associated subregime. Legend: Diffusive 1, ▲ (left column), $A = 4 \times 10^{-23}$ J, $r = 0.25$ μm, $0.1 \leqslant U \leqslant 10$ mm/s; (right column) $A = 8 \times 10^{-21}$ J, $U = 1$ mm/s, $0.1 \leqslant r \leqslant 0.5$ μm. Diffusive 2, ⬟, $h = 20$ μm, $\varphi = 0.3\%$, $L = 400$ μm, $A = 1 \times 10^{-24}$ J, $r = 2.5$ μm, $0.001 \leqslant U \leqslant 100$ mm/s. van der Waals 1, ◁ (topmost row), $2.5 \times 10^{-19} \leqslant A \leqslant 5 \times 10^{-19}$ J, $U = 2$ mm/s, $r = 0.125$ μm, $\xi_L = 544$; (second row from top) $5 \times 10^{-20} \leqslant A \leqslant 2.5 \times 10^{-17}$ J, $U = 1$ mm/s, $r = 0.25$ μm, $\xi_L = 68$; (middle row) $8 \times 10^{-21} \leqslant A \leqslant 1 \times 10^{-19}$ J, $U = 10$ mm/s, $r = 0.25$ μm, $\xi_L = 6.8$; (second row/point from bottom) $A = 5 \times 10^{-20}$ J, $U = 100$ mm/s, $r = 0.25$ μm, $\xi_L = 0.68$; (bottommost row/point) $A = 5 \times 10^{-19}$ J, $U = 0.1$ mm/s, $r = 2.5$ μm, $\xi_L = 0.078$; van der Waals 2, ● (top row/point), $A = 8 \times 10^{-21}$ J, $U = 0.1$ mm/s, $r = 2.5$ μm, $\xi_L = 0.078$; (middle row) $2 \times 10^{-22} \leqslant A \leqslant 5 \times 10^{-20}$ J, $U = 1$ mm/s, $r = 2.5$ μm, $\xi_L = 0.0078$; (bottom row) $7 \times 10^{-24} \leqslant A \leqslant 5 \times 10^{-20}$ J, $U = 10$ mm/s, $r = 2.5$ μm, $\xi_L = 0.00078$.

(ii) In the vdW 2 regime, where the capture layer $\delta < r$, we use a fixed value of U and relatively large r such that $\xi_L < 1$.

(iii) In the diffusive 1 regime, where the capture layer $\delta > r$, we employ fixed A and U, while changing r, L, and h in order to vary ξ_L (such that $\xi_L > 1$).

(iv) In the diffusive 2 regime, where the capture layer $\delta < r$, we use a fixed value of A, L, h, and relatively large r, while changing U in order to vary ξ_L (such that $\xi_L < 1$).

The plots in Fig. 8 provide examples of a numerical check of the theoretical predictions for both cases of the diffusive and van der Waals regimes. From these simulation results, noting the several orders of magnitude for which the scaling laws are obtained, with the right exponents, we may conclude that theory agrees very well with the numerics. For the two van der Waals regimes, 1 and 2, we recover well the expected prefactors. For the diffusive regimes, where only the exponents are predicted theoretically, we numerically found (i) diffusive regime 1, $S = (0.85 \pm 0.1)\xi_L^{1/3}$; (ii) diffusive regime 2, $S = (0.5 \pm 0.05)\xi_L$.

The plots in Fig. 9 provide a numerical check of another series of theoretical predictions, those related to Fig. 2, where ξ_L is a function of A/kT. This graph of the four subregimes is obtained in the presence of high salinity. To obtain Fig. 9, we performed simulations for different values of the parameters A/kT and ξ_L, and applied the different criteria based on the value of S to determine in which subregime each set of conditions lies. From these simulations, we could conclude that the theory leading to Fig. 2 agrees well with the numerics.

[1] E. Dressaire and A. Sauret, Clogging in microfluidic channels, Soft Matter **13**, 37 (2017).

[2] R. Mukhopadhyay, When microfluidic devices go bad, Anal. Chem. **77**, 429A (2005).

[3] T. van der Laar, A. ten Klooster, K. Schroen, and J. Sprakel, Transition state theory predicts clogging in microscale, Sci. Rep. **6**, 28450 (2016).

[4] C. Henry, J.-P. Minier, and G. Lefèvre, Towards a description of particulate fouling: From single particle deposition to clogging, Adv. Colloids Interface Sci. **185–186**, 34 (2012).

[5] H. M. Wyss, D. L. Blair, J. F. Morris, H. A. Stone, and D. A. Weitz, Mechanism for clogging in microchannels, Phys. Rev. E **74**, 061402 (2006).

[6] B. Dersoir, M. R. de Saint Vincent, M. Akbarian, and H. Tabuteau, Clogging of a single pore by colloidal particles, Microfluid. Nanofluid. **19**, 953 (2015).

[7] M. R. de Saint Vincent, M. Akbarian, and H. Tabuteau, Dynamics of colloid accumulation under flow over porous obstacles, Soft Matter **12**, 1041 (2016).

[8] P. Bacchin, W. Drekx, D. Veyret, K. Glucina, and P. Moulin, Clogging of microporous channel networks: Role of connectivity and tortuosity, Microfluid. Nanofluid. **17**, 85 (2014).

[9] Z. B. Sendekie and P. Bacchin, Colloidal jamming dynamics in microchannel bottlenecks, Langmuir **32**, 1478 (2016).

[10] M. Schoenitz, L. Grundemann, W. Augustin, and S. Scholl, Fouling in microstructured devices: A review, Chem. Commun. **51**, 8213 (2015).

[11] B. Mustin and B. Stoeber, Single layer deposition of polystyrene particles onto planar polydimethyl siloxane substrates, Langmuir **32**, 88 (2016).

[12] H. N. Unni and C. Yang, Colloidal particle deposition from electrokinetic flow in microfluidic channel, Electrophoresis **30**, 732 (2009).

[13] H. N. Unni and C. Yang, Kinetics of colloidal particle deposition to a solid surface from pressure driven microchannel flows, Can. J. Chem. Eng. **85**, 609 (2007).

[14] C. M. Cejas, F. Monti, M. Truchet, J. P. Burnouf, and P. Tabeling, Particle deposition kinetics of colloidal particles in microchannels at high ionic strength, Langmuir **33**, 6471 (2017).

[15] B. Dersoir, A. Schofield, and H. Tabuteau, Clogging transition induced by self infiltration in a slit pore, Soft Matter **13**, 2054 (2017).

[16] A. Sauret, E. C. Barney, A. Perro, E. Villermax, H. A. Stone, and E. Dressaire, Clogging by sieving in microchannels: Application to the the detection of contaminants in colloidal suspensions, Appl. Phys. Lett. **105**, 074101 (2014).

[17] Z. Adamczyk, *Particles and Interfaces, Interactions, Deposition, and Structure* (Academic Press, New York, 2006).

[18] M. V. Smoluchowski, Über brownsche molekularbewegung unter einwirkung äußerer kräfte und den zusammenhang mit der verallgemeinerten diffusionsgleichung, Ann. Phys. **353**, 1103 (1915).

[19] Z. Adamczyk, T. Dabros, J. Czarnecki, and T. V. de Ven, Particle transfer to solid surfaces, Adv. Colloid Interface Sci. **19**, 183 (1983).

[20] M. Elimelech, J. Gregory, X. Jia, and R. A. Williams, *Particle Deposition and Aggregation—Measurement in Modelling and Simulation*, edited by R. A. Williams (Elsevier, Amsterdam, 1995).

[21] H. Brenner, The slow motion of a sphere through a viscous fluid towards the plane, Chem. Eng. Sci. **16**, 242 (1961).

[22] M. A. Bevan and D. C. Prieve, Hindered diffusion of colloidal particles very near to the wall: Revisited, J. Chem. Phys. **113**, 1228 (2000).

[23] M. M. Fyrillas and K. K. Nomura, Diffusion and Brownian motion in Lagrangian coordinates, J. Chem. Phys. **126**, 164510 (2007).

[24] X. Z. Tang, A Lagrangian analysis of advection-diffusion equation for a three dimensional chaotic flow, Phys. Fluids **11**, 1418 (1999).

[25] J.-L. Thiffeault, Advection-diffusion in Lagrangian coordinates, Phys. Lett. A **309**, 415 (2003).

[26] B. H. Devkota and J. Imberger, Lagrangian modeling of advection-diffusion transport in open channel flow, Water Resour. Res. **45**, W12406 (2009).

[27] K. M. Yao, M. T. Habibian, and C. R. O'Melia, Waste and waste water filtration: Concepts and applications, Environ. Sci. Technol. **5**, 1105 (1971).

[28] N. Tufenkji and M. Elimelech, Breakdown of colloid infiltration theory: Rule of the secondary energy minimum and surface charge heterogeneities, Langmuir **21**, 841 (2005).

[29] V. G. Levich, *Physicochemical Hydrodynamics* (Prentice-Hall, Englewood Cliffs, NJ, 1962).

[30] D. P. Bakker, H. J. Busscher, and H. C. van der Mei, Bacterial deposition in a parallel plate and a stagnation point chamber:

Microbial adhesion mechanisms depend on the mass transport conditions, Microbiology **148**, 597 (2002).

[31] M. Lundqvist, J. Stigler, G. Elia, I. Lynch, T. Cedervall, and K. A. Dawson, Nanoparticle size and surface properties determine the protein corona with possible implications for biological impacts, Proc. Natl. Acad. Sci. USA **105**, 14265 (2008).

[32] J. Israelachvili, *Intermolecular and Surface Forces* (Elsevier, New York, 1991).

[33] F. L. Leite, C. Bueno, A. L. Da Roz, E. C. Zeimath, and O. N. Oliveira, Jr., Theoretical models for surface forces and adhesion and their measurement using atomic force microscopy, Int. J. Mol. Sci. **13**, 12773 (2012).

[34] J. Mahanty and B. W. Ninham, *Dispersion Forces* (Academic Press, New York, 1976).

[35] L. Bergstrom, Hamaker constants of inorganic materials, Adv. Colloid Interface Sci. **70**, 125 (1997).

[36] J. Israelachvili and G. E. Adams, Measurement of forces between two mica surfaces in aqueous electrolyte solutions in the range of 0-100 nm, J. Chem. Soc. Faraday Trans. **74**, 975 (1978).

[37] B. Ninham and V. Parsegian, van der Waals forces across triple-layer films, J. Phys. Chem. **52**, 4578 (1970).

[38] S. Pradhan, J. Hedberg, E. Blomberg, S. Wold, and I. Odnevall Wallinder, Effect of sonication on particle dispersion, administered dose and metal release of non-functionalized, non-inert metal nanoparticles, J. Nanopart. Res. **18**, 285 (2016).

[39] See Supplemental Material at http://link.aps.org/supplemental/10.1103/PhysRevE.98.062606 for additional experiments and the numerical simulation code.

[40] C. K. Choi, C. H. Margraves, and K. D. Kihm, Examination of near-wall hindered Brownian diffusion of nanoparticles: Experimental comparison to theories by Brenner (1961) and Goldman *et al.* (1967), Phys. Fluids **19**, 103305 (2007).

[41] N. B. Vicente, J. E. Diaz Zamboni, J. E. Adur, E. V. Paravani, and V. H. Casco, Photobleaching correction in fluorescence microscopy images, J. Phys.: Conf. Ser. **90**, 012068 (2007).

[42] P. Langevin, Sur la theorie du mouvement brownien, C. R. Acad. Sci. Paris **146**, 530 (1908); D. S. Lemons and A. Gythiel, Paul Langevin's 1908 paper On the theory of Brownian Motion, Am. J. Phys. **65**, 1079 (1997).

[43] P. Tabeling, *Introduction to Microfluidics* (Oxford University Press, Oxford, UK, 2005).